Weierstraß-Institut
für Angewandte Analysis und Stochastik

im Forschungsverbund Berlin e.V.

Preprint ISSN 0946 – 8633

Numerical simulation of heat transfer in materials with anisotropic thermal conductivity: A finite volume scheme to handle complex geometries

Jürgen Geiser[1], Olaf Klein[1] and Peter Philip[2]

submitted: 9th June 2005

[1] Weierstrass Institute
for Applied Analysis
and Stochastics
Mohrenstrasse 39
D-10117 Berlin
Germany
E-Mail: geiser@wias-berlin.de
klein@wias-berlin.de

[2] Institute for Mathematics
and its Applications (IMA)
University of Minnesota
400 Lind Hall
207 Church Street S.E.
Minneapolis, MN 55455-0436
USA
E-Mail: philip@ima.umn.edu

No. 1033

Berlin 2005

2000 *Mathematics Subject Classification.* 80A20 80M25 74S10 76R50 35J60 35J65 65M99 65Z05.

Key words and phrases. Numerical simulation. Heat transfer. Anisotropic diffusion. Anisotropic thermal conductivity. Finite volume method. Delaunay triangulation. Nonlinear elliptic PDE's.

2003 *Physics Abstract Classifications.* 02.60.Cb 44.05.+e 47.27.Te.

This work has been supported by the DFG Research Center MATHEON – "Mathematics for key technologies" (FZT 86) in Berlin and by the Institute for Mathematics and its Applications (IMA) in Minneapolis.

Edited by
Weierstraß-Institut für Angewandte Analysis und Stochastik (WIAS)
Mohrenstraße 39
10117 Berlin
Germany

Fax: + 49 30 2044975
E-Mail: preprint@wias-berlin.de
World Wide Web: http://www.wias-berlin.de/

Abstract

We devise a finite volume scheme for nonlinear heat transfer in materials with anisotropic thermal conductivity. We focus on the difficulties arising from the discretization of complex domains which are typical in the simulation of industrially relevant processes. For polyhedral domains in two dimensions, we consider Cartesian as well as cylindrical coordinates. Our finite volume scheme is based on unstructured constrained Delaunay triangulations of the domain. For simplicity, we assume that the thermal conductivity tensor has vanishing off-diagonal entries and that the anisotropy is independent of the temperature. We present numerical simulations, verifying our finite volume scheme in cases where a closed-form solution is available. Further results demonstrate the effectiveness of the method in computing the heat transfer in a complex growth apparatus used in crystal growth.

1 Introduction

Modeling and numerical simulation of heat transfer in complex apparatus have become powerful tools in aiding the design and optimization of numerous industrial processes such as crystal growth by the Czochralski method [DNR$^+$90] and by the physical vapor transport (PVT) method [KPS04] to mention just two examples. For materials with isotropic thermal conductivity, standard techniques are available, including the finite element method [CL91] (used in [DNR$^+$90]) and the finite volume method [EGH00] (used in [KPS04]). The extension of such standard methods to materials with anisotropic thermal conductivity can be straightforward for simple geometries (e.g. if the geometry admits a discretization into a structured grid of rectangles or parallelepipeds). However, the treatment of anisotropic materials within complex geometries as they are typical in industrial applications such as crystal growth (see Fig. 1) is generally much more involved. To the authors' knowledge, even for two-dimensional domains, all the methods previously described in the literature are restricted to simple classes of domains, need to be adapted to fit the type of anisotropy, or show instabilities for strongly anisotropic materials (see, e.g., [ABB98a, ABB98b, BV03, Fai91] and [EGH00, Sec. 11]).

Our goal is the formulation of a finite volume scheme that applies to apparatus geometries such as the one depicted in Fig. 1, consisting of several different material domains, some of which have anisotropic thermal conductivity. The scheme should be stable and accurate for any two-dimensional polyhedral domain discretized into a constrained Delaunay triangulation (see Sec. 3.1) such as provided by the grid generator *Triangle* [She96]. The scheme devised in our present article has the advantage of yielding accurate results without any further requirements with respect to the grid, even for very large anisotropy factors (in Sec. 4.3 we present numerical results for the domain of Fig. 1, where, in Ω_1, the material's thermal conductivity in the horizontal direction is 1000 times larger than in the vertical direction).

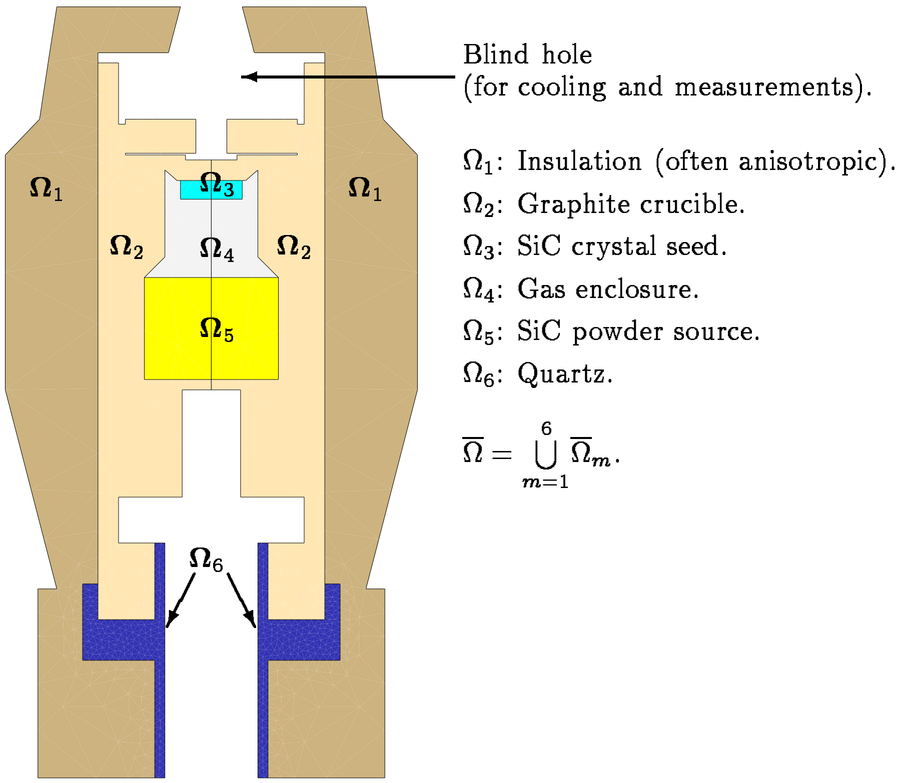

Figure 1: Axisymmetric domain representing a growth apparatus used in silicon carbide single crystal growth by physical vapor transport (PVT). The geometry is a modified version of [SSP04, Fig. 4].

We consider general two-dimensional polyhedral domains in both Cartesian and cylindrical coordinates (see Assumption (A-1) below). We will first develop the discretization in Cartesian coordinates, subsequently describing the necessary modifications for the case that the two-dimensional domain constitutes the circular projection of an axisymmetric domain in cylindrical coordinates (see Sec. 3.6). According to our aforementioned goals, in order to have the flexibility to discretize general polyhedral domains, we found our finite volume scheme on an unstructured constrained Delaunay triangulation (see Assumptions (DA-1) and (DA-3) in Sec. 3.1 below).

The paper is organized as follows: The mathematical model is stated in Sec. 2, the finite volume discretization is described in Sec. 3, followed by the presentation and discussion of numerical results in Sec. 4. The discretization in Sec. 3 is first carried out in Cartesian coordinates, the heart being the treatment of the anisotropic terms in Sec. 3.3. In Sec. 3.6, we describe the modification in the case of cylindrical coordinates. Section 4 is divided into three subsections: The tools used in the implementation are the contents of 4.1, the comparison of our numerical results with closed-form solutions is found in 4.2, and, in 4.3, we report on numerical results for the complex geometry of Fig. 1.

2 Mathematical model

Stationary heat conduction in potentially anisotropic materials is described by (see, e.g., [For01]):

$$-\operatorname{div}(K_m(\theta)\,\nabla\,\theta) = f_m \quad \text{in } \Omega_m \qquad (m \in M), \tag{2.1}$$

where $\theta \geq 0$ represents absolute temperature, the symmetric and positive definite matrix K_m represents the thermal conductivity tensor in material m, $f_m \geq 0$ represents heat sources in material m due to some heating mechanism, e.g. induction or resistance heating, Ω_m is the domain of material m, and M is a finite index set. We consider the case where the thermal conductivity tensor is a diagonal matrix with temperature-independent anisotropy, i.e.

$$K_m(\theta) = \big(\kappa^m_{i,j}(\theta)\big), \quad \text{where} \quad \kappa^m_{i,j}(\theta) = \begin{cases} \alpha^m_i\,\kappa^m_{\text{iso}}(\theta) & \text{for } i = j, \\ 0 & \text{for } i \neq j, \end{cases} \tag{2.2}$$

$\kappa^m_{\text{iso}}(\theta) > 0$ being the potentially temperature-dependent thermal conductivity of the isotropic case, and $\alpha^m_i > 0$ being anisotropy coefficients. For example, the growth apparatus used in silicon carbide single crystal growth by PVT are usually insulated by graphite felt, where the fibers are aligned in one particular direction, resulting in a thermal conductivity tensor of the form (2.2). We apply the finite volume scheme developed in the present paper to numerically investigate the influence of the anisotropy in the thermal insulation of PVT growth apparatus in [GKP05].

Throughout this paper, we make the following assumptions on the material domains Ω_m:

(A-1) $\overline{\Omega} = \bigcup_{m\in M} \overline{\Omega}_m$, $\Omega_{m_1} \cap \Omega_{m_2} = \emptyset$ for each $(m_1, m_2) \in M^2$ such that $m_1 \neq m_2$, and each of the sets Ω, Ω_m, $m \in M$, is a nonvoid, connected, polyhedral, bounded, and open subset of $\mathbb{R}^2$.

The temperature θ is assumed to be continuous throughout the entire domain $\overline{\Omega}$. Continuity of the normal component of the heat flux on the interface between different materials m_1 and m_2, $m_1 \neq m_2$, yields the following interface conditions, coupling the heat equations (2.1):

$$\big(K_{m_1}(\theta)\,\nabla\,\theta\big)\restriction_{\overline{\Omega}_{m_1}} \bullet\, \mathbf{n}_{m_1} = \big(K_{m_2}(\theta)\,\nabla\,\theta\big)\restriction_{\overline{\Omega}_{m_2}} \bullet\, \mathbf{n}_{m_1} \quad \text{on } \overline{\Omega}_{m_1} \cap \overline{\Omega}_{m_2}, \tag{2.3}$$

where $\restriction$ denotes restriction, and $\mathbf{n}_{m_1}$ denotes the unit normal vector pointing from material m_1 to material m_2.

We consider two types of outer boundary conditions, namely Dirichlet and Robin conditions. To that end, we decompose $\partial\Omega$ according to (A-2):

(A-2) Let Γ_{Dir} and Γ_{Rob} be relatively open polyhedral subsets of $\partial\Omega$ such that $\partial\Omega = \overline{\Gamma}_{\text{Dir}} \cup \overline{\Gamma}_{\text{Rob}}$, $\Gamma_{\text{Dir}} \cup \Gamma_{\text{Rob}} = \emptyset$.

The boundary conditions then read

$$\theta = \theta_{\mathrm{Dir}} \qquad \text{on } \overline{\Gamma}_{\mathrm{Dir}}, \tag{2.4a}$$

$$-\big(K_m(\theta)\,\nabla\,\theta\big) \bullet \mathbf{n}_m = \xi_m\,(\theta - \theta_{\mathrm{ext},m}) \qquad \text{a.e. on } \Gamma_{\mathrm{Rob}} \cap \partial\Omega_m,\ m \in M, \tag{2.4b}$$

where $\mathbf{n}_m$ is the outer unit normal to Ω_m, $\theta_{\mathrm{Dir}} \geq 0$ is the given temperature on Γ_{Dir}, $\theta_{\mathrm{ext},m} \geq 0$ is the given external temperature ambient to $\Gamma_{\mathrm{Rob}} \cap \partial\Omega_m$, and $\xi_m > 0$ is a transition coefficient.

We restrict ourselves to the simple interface and boundary conditions (2.3) and (2.4), respectively, since they suffice for our purpose of formulating and numerically verifying a finite volume scheme in situations with anisotropic thermal conductivity. For the isotropic case, many different interface and boundary conditions are considered in the finite volume schemes treated in [EGH00]. For finite volume schemes with nonlocal interface and boundary conditions due to diffuse-gray radiation between cavity surfaces, which are particularly relevant to high-temperature crystal growth applications, we refer to [Phi03, KP05].

In the case of transient heat conduction, the time derivative $\frac{\partial \varepsilon_m(\theta)}{\partial t}$ must be added in (2.1), where ε_m represents the internal energy of the respective material, and θ and f_m, in general, depend on time t. Since time dependence is decoupled from the anisotropy issues considered in this paper, we restrict ourselves to the stationary case. Extending the scheme to the transient case can be accomplished in the usual way, see, e.g. [EGH00, Ch. IV], [FL01, KP05].

3 Finite volume discretization

3.1 Discretization of the domains

Using a constrained Delaunay triangulation to discretize polyhedral domains, followed by a Voronoï construction to define finite volumes, is a well-known procedure (see [FL01, Sec. 3.2] and references therein). Here, we briefly review some definitions and properties that are subsequently used in the formulation of the finite volume scheme for the anisotropic case.

Following [FL01, Sec. 3.2], an admissible discretization of material domain Ω_m, $m \in M$, consists of a finite family $\Sigma_m := (\sigma_{m,i})_{i \in I_m}$ of subsets of Ω_m satisfying a number of assumptions, subsequently denoted by (DA-$*$).

Notation 3.1. For $d \in \{1,2\}$, let λ_d denote d-dimensional Lebesgue measure.

(DA-1) For each $m \in M$, $\Sigma_m = (\sigma_{m,i})_{i \in I_m}$ forms a finite conforming triangulation of Ω_m. In particular, for each $i \in I_m$, $\sigma_{m,i}$ is an open triangle. Moreover, letting $I := \bigcup_{m \in M} I_m$, $\Sigma := (\sigma_i)_{i \in I}$ forms a conforming triangulation of Ω.

(DA-2) For each $m \in M$, the triangulation $\Sigma_m = (\sigma_{m,i})_{i \in I_m}$ respects Γ_{Dir} and Γ_{Rob} in the sense that, for each $i \in I_m$, either $\lambda_1(\Gamma_{\text{Dir}} \cap \partial\sigma_{m,i}) = 0$ or $\lambda_1(\Gamma_{\text{Rob}} \cap \partial\sigma_{m,i}) = 0$.

For each $\sigma_{m,i}$, let $V(\sigma_{m,i}) = \{v^m_{i,j} : j \in \{1,2,3\}\}$ denote the set of vertices of $\sigma_{m,i}$, and let $V := \bigcup_{m \in M,\, i \in I_m} V(\sigma_{m,i})$ be the set of all vertices in the triangulation. One can then define the control volumes as the Voronoï cells with respect to the vertices. Using $\|\cdot\|_2$ to denote Euclidean distance, define

$$\text{for all } v \in V: \qquad \omega_v := \{x \in \Omega : \|x - v\|_2 < \|x - z\|_2 \text{ for each } z \in V \setminus \{v\}\}, \tag{3.1a}$$

$$\text{for all } m \in M: \quad \omega_{m,v} := \omega_v \cap \Omega_m, \quad V_m := \{z \in V : \omega_{m,z} \neq \emptyset\}. \tag{3.1b}$$

Letting $\mathcal{T} := (\omega_v)_{v \in V}$, $\mathcal{T}_m := (\omega_{m,v})_{v \in V_m}$, $m \in M$, $\mathcal{T}$ forms a partition of Ω, and $\mathcal{T}_m$ forms a partition of Ω_m.

Remark 3.2. Since $\mathcal{T}$ is a Voronoï discretization, each intersection $\partial\omega_v \cap \partial\omega_z$, $(v,z) \in V^2$, $v \neq z$, is contained in the set $\{x \in \Omega : \|v - x\|_2 = \|z - x\|_2\}$. In particular, $\frac{z-v}{\|z-v\|_2} = \mathbf{n}_{\omega_v}\restriction_{\partial_{\text{reg}}\omega_v \cap \partial_{\text{reg}}\omega_z}$, where ∂_{reg} denotes the regular boundary of a polyhedral set, i.e. the points of the boundary, where a unique outer unit normal vector exists, $\partial_{\text{reg}}\emptyset := \emptyset$; and $\mathbf{n}_{\omega_v}\restriction_{\partial_{\text{reg}}\omega_v \cap \partial_{\text{reg}}\omega_z}$ is the outer unit normal to ω_v restricted to the face $\partial_{\text{reg}}\omega_v \cap \partial_{\text{reg}}\omega_z$ (see Fig. 2).

Notation 3.3. If $A \subseteq \mathbb{R}^2$, then $\operatorname{conv} A$ denotes the convex hull of A. For each pair of points $(x,y) \in \mathbb{R}^2 \times \mathbb{R}^2$, let $[x,y] := \operatorname{conv}\{x,y\}$ denote the line segment between x and y.

(DA-3) For each $m \in M$, the triangulation Σ_m has the constrained Delaunay property: If $\tilde{V}_m := \bigcup_{i \in I_m} V(\sigma_{m,i})$; then, for each $(v,z) \in \tilde{V}_m^2$ such that $v \neq z$, the following conditions (a) and (b) are satisfied:

(a) If the boundaries of the Voronoï cells corresponding to v and z have a one-dimensional intersection, i.e. if $\lambda_1(\partial\omega_{m,v} \cap \partial\omega_{m,z}) \neq 0$, then $[v,z]$ is an edge of at least one $\sigma \in \Sigma_m$.

(b) If $[v,z]$ is an edge of at least one $\sigma \in \Sigma_m$, then the boundaries of the corresponding Voronoï cells have a nonempty intersection, i.e. $\partial\omega_{m,v} \cap \partial\omega_{m,z} \neq \emptyset$.

Also see Fig. 2, Rem. 3.4, and [FL01, Sec. 3.2].

Remark 3.4. Due to the two-dimensional setting, (DA-3) can be expressed equivalently in terms of the angles in the triangulation: For each $m \in M$, if γ is an interior edge of the triangulation Σ_m, and α and β are the angles opposite to γ, then $\alpha + \beta \leq \pi$. If $\gamma \subseteq \partial\Omega_m$ is a boundary edge of Σ_m, and α is the angle opposite γ, then $\alpha \leq \pi/2$.

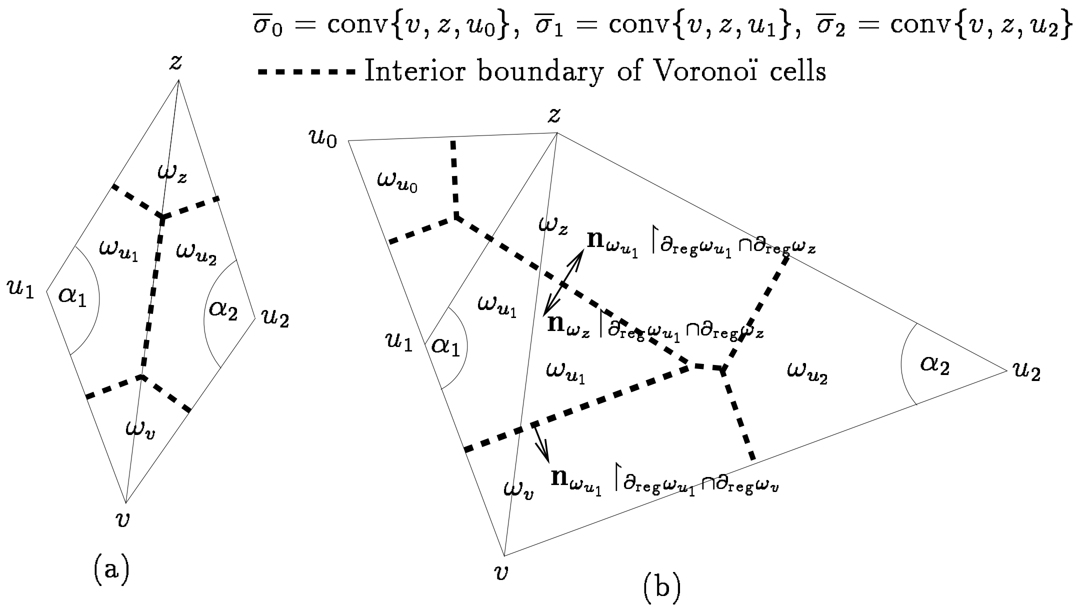

Figure 2: The pictures show the Voronoï cells of the triangulation vertices u_0, u_1, u_2, v, z. In (a), the triangulation violates the constrained Delaunay property ($\alpha_1 + \alpha_2 > \pi$, cf. (DA-3) and Rem. 3.4); in (b) the constrained Delaunay property is satisfied if, and only if, the edge $[v, z]$ is not a material interface ($\pi/2 < \alpha_1$, $\alpha_1 + \alpha_2 < \pi$).

The following Rem. 3.5 allows the incorporation of the interface condition (2.3) into the finite volume scheme (see (3.8) below).

Remark 3.5. Using Rem. 3.2, it is not hard to show that (DA-1) and (DA-3) imply the following assertions (a) and (b):

(a) For each $m \in M$, the set V_m defined in (3.1b) is identical to the set $\tilde{V}_m$ defined in (DA-3).

(b) Let Γ be a one-dimensional material interface: $\Gamma = \partial\Omega_m \cap \partial\Omega_{\tilde{m}}$, $\lambda_1(\Gamma) \neq 0$. For each $v \in V$, if some $\overline{\omega}_v$ has a one-dimensional intersection with the interface Γ, then it lies on both sides of the intersection; in other words, $\partial_{\text{reg}}\omega_{m,v} \cap \Gamma = \partial_{\text{reg}}\omega_{\tilde{m},v} \cap \Gamma$, in particular, $\lambda_1(\partial\omega_{m,v} \cap \Gamma) \neq 0$ if, and only if $\lambda_1(\partial\omega_{\tilde{m},v} \cap \Gamma) \neq 0$. However, Fig. 2(a) shows that this can generally not be expected in cases where the constrained Delaunay property is violated: If the edge $[v, w] =: \Gamma$ constitutes a material interface, then both $\overline{\omega}_{u_1}$ and $\overline{\omega}_{u_2}$ have one-dimensional intersections with Γ, but lie on just one side of Γ.

Integrating (2.1) over $\omega_{m,v}$ and applying the Gauss-Green integration theorem yields

$$-\int_{\partial\omega_{m,v}} (K_m(\theta)\, \nabla\, \theta) \bullet \mathbf{n}_{\omega_{m,v}} = \int_{\omega_{m,v}} f_m, \tag{3.2}$$

where $\mathbf{n}_{\omega_{m,v}}$ denotes the outer unit normal vector to $\omega_{m,v}$.

3.2 Approximation of integrals, interface and boundary conditions

The finite volume scheme is furnished by using the interface conditions (2.3) and boundary condition (2.4a) together with (3.2), and by approximating integrals by quadrature formulas. To approximate θ by a finite number of discrete unknowns θ_v, $v \in V$, precisely one value θ_v is associated with each control volume ω_v, where θ_v can be interpreted as $\theta(v)$ (cf. [FL01]).

On outer vertices $v \in V_{\text{Dir}} := V \cap \overline{\Gamma}_{\text{Dir}}$, the value of the solution is known from the Dirichlet condition (2.4a):

$$\theta_v = \theta_{\text{Dir}}(v) \quad \text{for each } v \in V_{\text{Dir}}. \tag{3.3}$$

It remains to formulate a system to determine θ_v for $v \in V_{\neg\text{Dir}} := V \setminus V_{\text{Dir}}$.

The boundary of each control volume $\omega_{m,v}$ can be decomposed into three parts:

$$\partial\omega_{m,v} = \big(\partial\omega_{m,v} \cap \Omega_m\big) \cup \big(\partial\omega_{m,v} \cap \partial\Omega\big) \cup \big(\partial\omega_{m,v} \cap (\partial\Omega_m \setminus \partial\Omega)\big), \tag{3.4}$$

where the first part lies in the interior of the material domain (dashed lines in Fig. 2), the second part coincides with part of the outer boundary, and the third part intersects material interfaces.

Remark 3.6. Simple geometric considerations show that the conditions (DA-1) and (DA-3) guarantee that the discretization $\mathcal{T}$ respects interfaces and outer boundaries, and that there is a vertex $v \in V$ in each of the integration domains $\omega_{m,v}$ occurring in (3.4). More precisely:

(a) For each $v \in V$: If there is $m \in M$ and an edge $[a, b]$ of a simplex of Σ_m such that $[a, b] \subseteq \partial\Omega_m$ and $\lambda_1(\overline{\omega}_v \cap [a, b]) \neq 0$, then $v = a$ or $v = b$.

(b) For each $v \in V$, $m \in M$: If $\omega_{m,v} \neq \emptyset$, then $v \in \overline{\omega}_{m,v}$. In particular, if $(m, \tilde{m}) \in M^2$, $\omega_{m,v} \neq \emptyset$, and $\omega_{\tilde{m},v} \neq \emptyset$, then $v \in \overline{\omega}_{m,v} \cap \overline{\omega}_{\tilde{m},v}$.

However, note that Rem. 3.6(a),(b) can generally not be expected for triangulations that violate the constrained Delaunay property: For example, if, in Fig. 2(b), the edge $[v, w]$ constitutes a material interface, say $\Omega_1 := \sigma_1$, $\Omega_2 := \sigma_2$, $[v, w] = \partial\Omega_1 \cap \partial\Omega_2$, then $\omega_{1,u_1} \neq \emptyset$ and $\omega_{2,u_1} \neq \emptyset$, but $u_1 \notin \overline{\omega}_{2,u_1}$.

By (DA-2) and by Rem. 3.6(a), control volumes $\overline{\omega}_v$ of non-Dirichlet vertices $v \in V_{\neg\text{Dir}}$ can not have one-dimensional intersections with Γ_{Dir}. Thus, for $v \in V_{\neg\text{Dir}}$, up to null sets with respect to λ_1, (3.4) reduces to

$$\partial\omega_{m,v} = \big(\partial\omega_{m,v} \cap \Omega_m\big) \cup \big(\partial\omega_{m,v} \cap \Gamma_{\text{Rob}}\big) \cup \big(\partial\omega_{m,v} \cap (\partial\Omega_m \setminus \partial\Omega)\big). \tag{3.5}$$

We proceed by employing the Robin condition (2.4b) on $\partial\omega_{m,v} \cap \Gamma_{\text{Rob}}$ followed by the approximations $\theta \approx \theta_v$ and $\theta_{\text{ext},m,v} \approx \big(\lambda_1(\partial\omega_{m,v} \cap \Gamma_{\text{Rob}})\big)^{-1} \cdot \int_{\partial\omega_{m,v} \cap \Gamma_{\text{Rob}}} \theta_{\text{ext},m}$, the second of which will be further discussed in Section 3.4 below:

$$-\int_{\partial\omega_{m,v}\cap\Gamma_{\text{Rob}}} (K_m(\theta)\,\nabla\,\theta) \bullet \mathbf{n}_{\omega_{m,v}} = \int_{\partial\omega_{m,v}\cap\Gamma_{\text{Rob}}} \xi_m\,(\theta - \theta_{\text{ext},m}) \approx \xi_m\,\big(\theta_v - \theta_{\text{ext},m,v}\big)\,\lambda_1(\partial\omega_{m,v}\cap\Gamma_{\text{Rob}}). \tag{3.6}$$

In the next step, we combine terms of the form $\int_{\partial\omega_{m,v}\cap(\partial\Omega_m\setminus\partial\Omega)}(K_m(\theta)\,\nabla\,\theta)\bullet \mathbf{n}_{\omega_{m,v}}$ by using the interface conditions (2.3). The set $\partial\omega_{m,v}\cap(\partial\Omega_m\setminus\partial\Omega)$ is decomposed further into the intersections with the boundaries of all the particular material domains. Up to λ_1-null sets:

$$\partial\omega_{m,v}\cap(\partial\Omega_m\setminus\partial\Omega) = \bigcup_{\tilde{m}\in M\setminus\{m\}} \partial\omega_{m,v}\cap\partial\Omega_m\cap\partial\Omega_{\tilde{m}}. \tag{3.7}$$

According to Rem. 3.5, for each $(m,\tilde{m})\in M^2$ with $m\neq\tilde{m}$, one has $\lambda_1(\partial\omega_{m,v}\cap\partial\Omega_m\cap\partial\Omega_{\tilde{m}})\neq 0$ if, and only if, $\lambda_1(\partial\omega_{\tilde{m},v}\cap\partial\Omega_m\cap\partial\Omega_{\tilde{m}})\neq 0$. This justifies the second equality in the following computation (3.8). For each $v\in V_{\neg\text{Dir}}$:

$$\begin{aligned}
&-\sum_{m\in M}\int_{\partial\omega_{m,v}\cap(\partial\Omega_m\setminus\partial\Omega)}(K_m(\theta)\,\nabla\,\theta)\bullet \mathbf{n}_{\omega_{m,v}}\\
&\overset{(3.7)}{=} -\sum_{m\in M}\sum_{\tilde{m}\in M\setminus\{m\}}\int_{\partial\omega_{m,v}\cap\partial\Omega_m\cap\partial\Omega_{\tilde{m}}}(K_m(\theta)\,\nabla\,\theta)\bullet \mathbf{n}_{\omega_{m,v}}\\
&= -\sum_{\substack{(m,\tilde{m})\in M^2:\\ m\neq\tilde{m},\\ \lambda_1(\partial\omega_{m,v}\cap\partial\Omega_m\cap\partial\Omega_{\tilde{m}})\neq 0}}\Bigg(\int_{\partial\omega_{m,v}\cap\partial\Omega_m\cap\partial\Omega_{\tilde{m}}}(K_m(\theta)\,\nabla\,\theta)\bullet \mathbf{n}_{\omega_{m,v}}\\
&\qquad\qquad + \int_{\partial\omega_{\tilde{m},v}\cap\partial\Omega_m\cap\partial\Omega_{\tilde{m}}}(K_{\tilde{m}}(\theta)\,\nabla\,\theta)\bullet \mathbf{n}_{\omega_{\tilde{m},v}}\Bigg) \overset{(2.3)}{=} 0.
\end{aligned} \tag{3.8}$$

3.3 Approximation of heat flux term, anisotropy

Notation 3.7. For each $m\in M$ and each $(v,w)\in M^2$, let $\gamma_{m,v,w} := \partial\omega_{m,v}\cap\partial\omega_{m,w}$ denote the interface of the two Voronoï cells inside the material domain Ω_m (of course, in general, $\gamma_{m,v,w}$ can be empty).

To approximate the heat flux integrals $\int_{\partial\omega_{m,v}\cap\Omega_m}(K_m(\theta)\,\nabla\,\theta)\bullet \mathbf{n}_{\omega_{m,v}}$, the set $\partial\omega_{m,v}\cap\Omega_m$ is also partitioned further, namely into the interfaces with all neighboring Voronoï cells. Up to null sets with respect to λ_1:

$$\partial\omega_{m,v}\cap\Omega_m = \bigcup_{w\in\text{nb}_m(v)}\gamma_{m,v,w}, \tag{3.9}$$

where $\text{nb}_m(v) := \{w\in V_m\setminus\{v\} : \lambda_1(\gamma_{m,v,w})\neq 0\}$ is the set of m-neighbors of v. For example, in Fig. 3, $\partial\omega_{1,v}$ is decomposed into γ_{1,v,u_1}, $\gamma_{1,v,w}$, and γ_{1,v,u_2}.

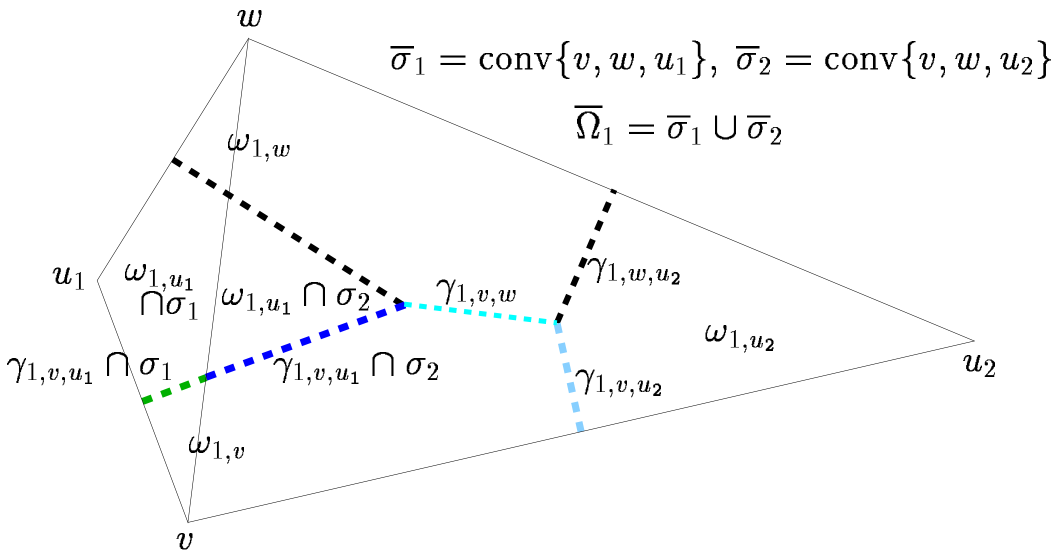

Figure 3: Illustration of the decomposition of $\partial\omega_{1,v}$.

The decomposition (3.9) reduces our task to approximating $(K_m(\theta)\,\nabla\,\theta) \bullet \mathbf{n}_{\omega_{m,v}}$ on $\gamma_{m,v,w}$. According to the assumed form (2.2) of the $K_m(\theta)$, the approximation can be broken down into two parts: (a) Approximation of the temperature-dependent, isotropic part. (b) Approximation of the temperature-independent, anisotropic part.

Approximation of the temperature-dependent, isotropic part

We approximate $\kappa^m_{\text{iso}}(\theta)$ on $\gamma_{m,v,w}$ by the arithmetic mean

$$\kappa^m_{\text{iso}}(\theta)\restriction_{\gamma_{m,v,w}} \approx \frac{1}{2}\left(\kappa^m_{\text{iso}}(\theta_v) + \kappa^m_{\text{iso}}(\theta_w)\right). \tag{3.10}$$

Other approximations instead of (3.10) are available through using the antiderivative of κ^m_{iso} or by using upwind (s. [FL01, Sec. 6.4]). While the theoretical results in [FL01] establish desirable stability properties for these approximations in the isotropic case, according to our numerical results presented in Sec. 4.3 below, the simple approximation (3.10) works sufficiently well for our purposes.

Approximation of the temperature-independent, anisotropic part

It remains to approximate $(A_m\,\nabla\,\theta) \bullet \mathbf{n}_{\omega_{m,v}}$ on $\gamma_{m,v,w}$, where A_m is the constant diagonal matrix

$$A_m = (a^m_{i,j}), \qquad a^m_{i,j} := \begin{cases} \alpha^m_i & \text{for } i = j, \\ 0 & \text{for } i \neq j. \end{cases} \tag{3.11}$$

The idea is to devise the approximation such that it is exact provided that θ is affine on each $\sigma \in \Sigma$ and provided that Σ has the strong Delaunay property (all angles are less than or equal to $\pi/2$). If θ is affine on $\sigma \in \Sigma$, then

$$\nabla\,\theta\restriction_\sigma = \sum_{v\in V(\sigma)} \theta(v)\;\nabla\,\phi_{\sigma,v}, \tag{3.12}$$

where $\phi_{\sigma,v} : \sigma \longrightarrow [0,1]$, $v \in V(\sigma)$, are the affine coordinates on the triangle σ with respect to its 3 vertices.

Given $m \in M$, $(v,w) \in V_m^2$, $v \neq w$, such that $[v,w]$ is an edge of some $\sigma \in \Sigma_m$, let

$$\Sigma_{m,v,w} := \big\{\sigma \in \Sigma_m : \{v,w\} \subseteq V(\sigma)\big\} \tag{3.13}$$

be the set of triangles in Σ_m having $[v,w]$ as an edge. Since Σ_m is a conforming triangulation of Ω_m by (DA-1), if $[v,w]$ is a boundary edge, then $\Sigma_{m,v,w}$ has precisely one element; otherwise, it has precisely two elements, lying on different sides of $[v,w]$. For each $\sigma \in \Sigma_{m,v,w}$, let $H_{v,w,\sigma}$ be the half-space that lies on the same side of the line through $[v,w]$ as σ. Even though (DA-3) guarantees $\lambda_1(\gamma_{m,v,w}) \neq 0$, Fig. 3 shows that $\gamma_{m,v,w}$ can lie entirely on one side of $[v,w]$. However, letting

$$\Sigma_{\gamma_{m,v,w}} := \big\{\sigma \in \Sigma_{m,v,w} : \lambda_1(H_{v,w,\sigma} \cap \gamma_{m,v,w}) \neq 0\big\}, \tag{3.14}$$

we can decompose $\gamma_{m,v,w}$ according to

$$\gamma_{m,v,w} = \bigcup_{\sigma\in\Sigma_{\gamma_{m,v,w}}} \overline{\sigma} \cap \gamma_{m,v,w}. \tag{3.15}$$

For example, in Fig. 3, $\gamma_{1,v,w}$ is decomposed into $\overline{\sigma}_1 \cap \gamma_{1,v,w}$ and $\overline{\sigma}_2 \cap \gamma_{1,v,w}$.

Using (3.12) together with Rem. 3.2 yields, for each $\sigma \in \Sigma_{\gamma_{m,v,w}}$:

$$(A_m \nabla\,\theta)\restriction_\sigma \bullet\, \mathbf{n}_{\omega_v}\restriction_{\gamma_{m,v,w}} = \sum_{\tilde v\in V(\sigma)} \theta(\tilde v)\,(A_m \nabla\,\phi_{\sigma,\tilde v}) \bullet \frac{w-v}{\|w-v\|_2}. \tag{3.16}$$

If we were to assume that $\mathcal{T}_m$ is an *A_m-orthogonal grid* as defined in [ABB98a], i.e. $\gamma_{m,v',w'} \bullet A_m(v'-w') = 0$ holds for all $v', w' \in \tilde V_m$ such that $[v', z']$ is an edge of at least one $\sigma \in \Sigma_m$, then we would have the relations $A_m \nabla\,\phi_{\sigma,v} \bullet (w-v) = -\|A_m(w-v)\|_2/\|w-v\|_2$, $A_m \nabla\,\phi_{\sigma,w} \bullet (w-v) = \|A_m(w-v)\|_2/\|w-v\|_2$, and $A_m \nabla\,\phi_{\sigma,u} \bullet (w-v) = 0$ for $u \in V(\sigma) \setminus \{v,w\}$. These relations would imply

$$(A_m \nabla\,\theta)\restriction_\sigma \bullet\, \mathbf{n}_{\omega_v}\restriction_{\gamma_{m,v,w}} = \frac{\theta(w)-\theta(v)}{\|w-v\|_2}\,\frac{\|A_m(w-v)\|_2}{\|w-v\|_2}, \tag{3.17}$$

corresponding to the approximation used in [EGH00, Sec. 11.1] under the A_m-orthogonality assumption. We also note that the approximation considered in [Fai91] reduces to (3.17) for an A_m-orthogonal Voronoï grid. In the usual isotropic case, where $\alpha_1^m = \alpha_2^m = 1$, the second factor on the right-hand side of (3.17) becomes equal to 1, resulting in the usually used approximation of the isotropic case.

Providing a grid Σ_m such that the corresponding $\mathcal{T}_m$ is A_m-orthogonal would allow to use the simpler approximation in (3.17) that only depends on the two values of θ in v and w, but, in contrast to (3.16), not on the value of θ in the third corner of σ. Unfortunately, for $\alpha_1 \neq \alpha_2$, A_m-orthogonality of $\mathcal{T}_m$ only holds if, for all Voronoï cells $\omega_{m,v}$, the part of the boundary $\partial\omega_{m,v}$ lying inside Ω_m consists only of horizontal or vertical line segments. This is a quite strong restriction for the mesh Σ_m, which could be avoided if, in the definition (3.1) of the Voronoï cells, one were to replace the Euclidean distance with the norm $\|\cdot\|_{A_m^{-1}}$ given by $\|v\|_{A_m^{-1}} := \sqrt{A_m^{-1}v \bullet v}$ for all vectors v. However, this would entail many additional difficulties for practical computations, as, for example, many formulas had to be adapted, and, more importantly, when dealing with different anisotropy values in the different Ω_m, one had to find a way for the grid generator to provide a grid Σ for Ω such that, for each $m \in M$, the subgrid Σ_m of Ω_m is appropriate for dealing with Voronoï cells defined with respect to the norm $\|\cdot\|_{A_m^{-1}}$. To avoid these additional problems that arise if one wants to ensure that (3.17) constitutes an accurate approximation, we prefer to use the slightly more complicated formula (3.16).

Combination of the temperature-dependent and temperature-independent parts

Combining the approximations of the temperature-dependent and the temperature-independent parts, we are now in a position to state our approximation of the heat flux integral $\int_{\gamma_{m,v,w}} (K_m(\theta)\nabla\theta) \bullet \mathbf{n}_{\omega_{m,v}}$. Combining (3.10), (3.15), and (3.16) yields

$$\begin{aligned}
&\int_{\gamma_{m,v,w}} (K_m(\theta)\nabla\theta) \bullet \mathbf{n}_{\omega_{m,v}} \\
&\approx \sum_{\sigma\in\Sigma_{\gamma_{m,v,w}}} \frac{1}{2}\left(\kappa_{\text{iso}}^m(\theta_v) + \kappa_{\text{iso}}^m(\theta_w)\right) \\
&\qquad \sum_{\tilde{v}\in V(\sigma)} \theta_{\tilde{v}}\left(A_m\nabla\phi_{\sigma,\tilde{v}}\right) \bullet \frac{w-v}{\|w-v\|_2}\,\lambda_1(H_{v,w,\sigma}\cap\gamma_{m,v,w}).
\end{aligned} \tag{3.18}$$

Remarks on triangulations involving obtuse angles

Consider the case where the triangulation Σ_m satisfies the constrained Delaunay property, but not the strong Delaunay property, i.e. where there is an interior edge such as $[v, w]$ in Fig. 3, with opposing angles α_1, α_2, $\pi/2 < \alpha_1$, $\alpha_1 + \alpha_2 \leq \pi$.

Then approximation (3.18) is generally *not* exact for piecewise affine θ even if $\kappa_{\text{iso}}^m \equiv 1$ and A_m is isotropic. For instance, in Fig. 3, on $\sigma_2 \cap \gamma_{1,v,w}$, the flux $(A_m\nabla\theta) \bullet \mathbf{n}_{\omega_v}\restriction_{\gamma_{m,v,u_1}}$ is approximated by $(A_m\nabla\theta)\restriction_{\sigma_1} \bullet \mathbf{n}_{\omega_v}\restriction_{\gamma_{m,v,u_1}}$, which is, in general, different from $(A_m\nabla\theta)\restriction_{\sigma_2} \bullet \mathbf{n}_{\omega_v}\restriction_{\gamma_{m,v,u_1}}$. One could modify (3.18) to be always exact for piecewise affine θ, albeit at the cost of making the implementation of the scheme more difficult. The simpler approximation used here, which is used in many papers dealing with finite volume schemes (see, e.g., [EGH00, FKL01]), is vindicated in the light of the numerical results presented in Sec. 4 below.

At this point, we would like to draw attention to an algorithmic pitfall that can arise when implementing formula (3.18) in the presence of both anisotropy and obtuse triangles. Let σ_1 and σ_2 be triangles belonging to Σ_m such that $[v,w]$ is a common edge of σ_1 and σ_2. According to (3.14), this means $\Sigma_{m,v,w} = \{\sigma_1, \sigma_2\}$. When implementing (3.18), one is faced with the task of computing $\lambda_1(H_{v,w,\sigma} \cap \gamma_{m,v,w})$, i.e. the length of $\gamma_{m,v,w}$ on both sides of $[v,w]$, where we recall that $\gamma_{m,v,w}$ is the interface between the Voronoï cells $\omega_{m,v}$ and $\omega_{m,w}$. Program packages suitable for the implementation of finite volume schemes such as *pdelib* [FKL01] provide functions that compute approximations of (3.18) using loops over all relevant pairs $([v,w],\sigma)$ and approximations $\lambda_{m,v,w,\sigma}$ of $\lambda_1(H_{v,w,\sigma} \cap \gamma_{m,v,w})$.

If the angles in σ_1 and σ_2 that are opposite to $[v,w]$ are both acute, then $\gamma_{m,v,w}$ has parts of positive length on both sides of $[v,w]$, and the approximations λ_{m,v,w,σ_1} and λ_{m,v,w,σ_2} as computed by *pdelib* are quite accurate. However, if one of the angles, say the one in σ_1 as in the situation depicted in Fig. 3, is obtuse, then $\gamma_{m,v,w}$ lies entirely on one side of $[v,w]$ such that $\lambda_1(H_{v,w,\sigma_1} \cap \gamma_{m,v,w}) = 0$, and the approximations λ_{m,v,w,σ_1} and λ_{m,v,w,σ_2} as provided by *pdelib* are no longer good approximations of $\lambda_1(H_{v,w,\sigma_1} \cap \gamma_{m,v,w})$ and $\lambda_1(H_{v,w,\sigma_2} \cap \gamma_{m,v,w})$, respectively. In fact, λ_{m,v,w,σ_1} will be *negative* and λ_{m,v,w,σ_2} will be *larger* than $\lambda_1(H_{v,w,\sigma_2} \cap \gamma_{m,v,w})$ such that the sum gives the correct value $\lambda_{m,v,w,\sigma_1} + \lambda_{m,v,w,\sigma_2} = \lambda_1(H_{v,w,\sigma_2} \cap \gamma_{m,v,w})$. In the isotropic situation, the behavior of the *pdelib* functions is still quite appropriate, since, in this case, the factor in front of $\lambda_1(H_{v,w,\sigma_1} \cap \gamma_{m,v,w})$ and the factor in front of $\lambda_1(H_{v,w,\sigma_2} \cap \gamma_{m,v,w})$ in (3.18) are both equal to $\frac{\theta(w)-\theta(v)}{\|w-v\|_2}$. Thus, multiplying with λ_{m,v,w,σ_1} for σ_1 and with λ_{m,v,w,σ_2} for σ_2 and summing up the results afterwards leads to a good approximation of the last line in (3.18). However, in the anisotropic situation, the factors in front of $\lambda_1(H_{v,w,\sigma_1} \cap \gamma_{m,v,w})$ and $\lambda_1(H_{v,w,\sigma_2} \cap \gamma_{m,v,w})$ are different. Hence, in order to get an accurate implementation of (3.18), in the *pdelib* loops over the relevant pairs $([v,w],\sigma)$, one can no longer multiply by the standard *pdelib* approximations $\lambda_{m,v,w,\sigma}$. For example, in the abovedescribed situation, one has to use 0 instead of λ_{m,v,w,σ_1}, and one has to use $\lambda_{m,v,w,\sigma_1} + \lambda_{m,v,w,\sigma_2}$ instead of λ_{m,v,w,σ_2}.

3.4 Approximation of the source term and of the external temperature

For the approximation of the source term, assuming that the f_m are at least integrable, let

$$f_{m,v} \approx \frac{\int_{\omega_{m,v}} f_m}{\lambda_2(\omega_{m,v})} \tag{3.19}$$

be a suitable approximation on $\omega_{m,v}$. In general, the choice will depend on the regularity of f_m (for f_m continuous, one might choose $f_{m,v} := f_m(v)$, but $f_{m,v} := (\lambda_2(\omega_{m,v}))^{-1} \cdot \int_{\omega_{m,v}} f_m$ for a general $f_m \in L^1(\Omega_m)$). However, a suitable approximation should satisfy

$$\left(f_{m,v}\, \lambda_2(\omega_{m,v}) - \int_{\omega_{m,v}} f_m \right) \to 0 \quad \text{for} \quad \text{diam}(\omega_{m,v}) \to 0. \tag{3.20}$$

Similarly, depending on the regularity of the external temperature $\theta_{\text{ext},m}$, in the approximation of the Robin boundary condition, one may choose $\theta_{\text{ext},m,v} := \theta_{\text{ext},m}(v)$, $\theta_{\text{ext},m,v} := (\lambda_1(\partial\omega_{m,v} \cap \Gamma_{\text{Rob}}))^{-1} \cdot \int_{\partial\omega_{m,v} \cap \Gamma_{\text{Rob}}} \theta_{\text{ext},m}$, or any other suitable approximation such that

$$\left(\theta_{\text{ext},m,v}\, \lambda_1(\partial\omega_{m,v} \cap \Gamma_{\text{Rob}}) - \int_{\partial\omega_{m,v} \cap \Gamma_{\text{Rob}}} \theta_{\text{ext},m} \right) \to 0 \quad \text{for} \quad \text{diam}(\omega_{m,v}) \to 0. \tag{3.21}$$

3.5 The finite volume scheme

At this point, all preparations are in place to state the finite volume scheme in (3.22) below. The terms in (3.22b) arise from (3.2) after summing over $m \in M$, using the decompositions (3.5), (3.7), (3.9), (3.15), as well as (3.8), and employing the approximations (3.6), (3.18), and (3.19), respectively. One is seeking a nonnegative solution $(\theta_v)_{v \in V}$ to the following nonlinear system:

$$\theta_v = \theta_{\text{Dir}}(v) \quad \text{for each } v \in V_{\text{Dir}}, \tag{3.22a}$$

$$\begin{aligned} 0 = {} & \sum_{m \in M} \xi_m \left(\theta_v - \theta_{\text{ext},m,v} \right) \lambda_1(\partial\omega_{m,v} \cap \Gamma_{\text{Rob}}) \\ & - \sum_{m \in M} \sum_{w \in \text{nb}_m(v)} \frac{1}{2} \left(\kappa_{\text{iso}}^m(\theta_v) + \kappa_{\text{iso}}^m(\theta_w) \right) \\ & \qquad \sum_{\sigma \in \Sigma_{\gamma_{m,v,w}}} \sum_{\tilde{v} \in V(\sigma)} \theta_{\tilde{v}} \left(A_m \nabla \phi_{\sigma,\tilde{v}} \right) \bullet \frac{w - v}{\|w - v\|_2} \lambda_1(H_{v,w,\sigma} \cap \gamma_{m,v,w}) \\ & - \sum_{m \in M} f_{m,v}\, \lambda_2(\omega_{m,v}) \quad \text{for each } v \in V_{\neg\text{Dir}} = V \setminus V_{\text{Dir}}. \end{aligned} \tag{3.22b}$$

3.6 Modifications for the axisymmetric case

Suppose that each material domain Ω_m, $m \in M$, is axisymmetric, and, in cylindrical coordinates (r, ϑ, z), θ and each f_m, $m \in M$, are independent of the angular coordinate ϑ. Starting with the model equations (2.1), (2.3), and (2.4) in three dimensions, one can then use the circular projection $(r, \vartheta, z) \mapsto (r, z)$ to reduce the model as well as the finite volume scheme to two dimensions.

It was shown in [Phi03, Sec. 3.6] how symmetry conditions together with a change of variables can be used to reduce the space dimension in a finite volume scheme. In the case of cylindrical coordinates, the change of variables merely yields a factor r in the integrands occurring in (3.6), (3.8), (3.18), and (3.19), and thus in the corresponding terms in (3.22b).

4 Numerical experiments

4.1 Implementation

In the following Sections 4.2 and 4.3, we present numerical results obtained using the axisymmetric version of scheme (3.22) (cf. Sec. 3.6). The scheme was implemented as part of our software *WIAS-HiTNIHS*[1] which is based on the program package *pdelib* [FKL01]. In particular, *pdelib* uses the grid generator *Triangle* [She96] to produce constrained Delaunay triangulations of the domains, and it uses the sparse matrix solver *PARDISO* [SGF00, SG04] to solve the linear system arising from the linearization of (3.22) via Newton's method. The Dirichlet condition (3.22a) is implemented employing the penalty method.

4.2 Comparison with closed-form solutions

4.2.1 Single-material domain

For the verification of our finite volume scheme, we consider the following axisymmetric Dirichlet problem, written in cylindrical coordinates (r, z) in the domain $\Omega = \{(r, z) : 0 < r < 0.2, -0.2 < z < 0.2\}$:

$$-\frac{1}{r}\frac{\partial}{\partial r}\left(r\,\alpha_r\,\frac{\partial\theta}{\partial r}\right) - \frac{\partial}{\partial z}\left(\alpha_z\,\frac{\partial\theta}{\partial z}\right) = 0 \qquad \text{in } \Omega, \tag{4.1a}$$

$$\theta(r, z) = \theta_{\text{Dir}}(r, z) := \frac{1}{2}\frac{1}{\alpha_r}r^2 - \frac{1}{\alpha_z}z^2 \qquad \text{on } \partial\Omega. \tag{4.1b}$$

The Dirichlet problem (4.1) has the obvious closed-form solution

$$\theta(r, z) = \frac{1}{2}\frac{1}{\alpha_r}r^2 - \frac{1}{\alpha_z}z^2 \quad \text{on } \overline{\Omega}. \tag{4.2}$$

We present the results of two numerical solutions of (4.1), one with $(\alpha_r, \alpha_z) = (1, 10)$ and one with $(\alpha_r, \alpha_z) = (10, 1)$. In both cases, the numerical solution is computed using our finite volume scheme (3.22), modified for the axisymmetric case as described in Sec. 3.6. We vary the fineness of the grid, subsequently referred to as grid level l, where a higher level means a finer grid. In practice, we use the grid generator *Triangle* [She96] to control the fineness of the grid: If $\Sigma^l = (\sigma_i^l)_{i \in I^l}$ denotes the triangulation of Ω for grid level l, then *Triangle* guarantees that the area of the triangles σ_i^l is bounded by our prescribed value A^l:

$$\lambda_2(\sigma_i^l) \leq A^l \quad \text{for each } i \in I^l. \tag{4.3}$$

We calculate the discrete L_2-error $\epsilon_{L_2}^l$ between the numerical solution θ_{num}^l of grid

[1] **High Temperature Numerical Induction Heating Simulator**; pronunciation: ~hit-nice.

level l and the exact solution θ given by (4.2):

$$\epsilon_{L_2}^l := \sqrt{\sum_{v \in V^l} \mathrm{vol}(\omega_v^l)\big(\, \theta_{\mathrm{num}}^l(v) - \theta(v)\,\big)^2}\,, \tag{4.4}$$

where $v \in V^l$ are the vertices of the triangulation of grid level l, and $\mathrm{vol}(\omega_v^l) := \int_{\omega_v^l} r\, \mathrm{d}r\mathrm{d}z$ is the r-weighted area of the Voronoï cell corresponding to the vertex v. To determine the order of our numerical scheme, for grid levels $l \geq 1$, we define the numerical convergence rate $\rho_{L_2}^l$ as follows (cf. [Krö97, LeV02]):

$$\rho_{L_2}^l := \big(\ln(\epsilon_{L_2}^l) - \ln(\epsilon_{L_2}^{l-1})\big) / \big(\ln(h^l) - \ln(h^{l-1})\big), \tag{4.5}$$

where h^l is the maximal edge length actually occurring in grid level l:

$$h^l := \max\big\{\|v - z\|_2 : \, [v, z] \text{ is edge of } \sigma_i^l, \; i \in I^l\big\}. \tag{4.6}$$

Tables 1 and 2 show the dependence of the L_2-error $\epsilon_{L_2}^l$ and of the numerical convergence rate $\rho_{L_2}^l$ on the grid level l as computed for our two numerical solutions of (4.1): We choose $A^0 := 4 \cdot 10^{-5}$, $A^l := (1/4)^l A^0$, $l \in \{0, \dots, 4\}$. As described above, the grid generator then guarantees (4.3). For each grid level l, we determine the actually occurring maximal edge length h^l according to (4.6). We find that we have the approximate relation $2\sqrt{A^l} \approx h^l$ (see values for h^l in Tables 1 and 2). The case $(\alpha_r, \alpha_z) = (1, 10)$ is depicted in Table 1, whereas the case $(\alpha_r, \alpha_z) = (10, 1)$ is depicted in Table 2. In both experiments, one can observe second order convergence: The error is approximately proportional to the square of the maximal edge length in the space discretization. This coincides with theoretical results in [Bey98, CLZ02], where, for a finite volume approximation of an isotropic elliptic equation with an $H^2(\Omega)$ solution (in [Bey98]) or with a differentiable right-hand side (in [CLZ02]), a second order convergence is proved.

level l	number of triangles	max edge length h^l	L_2-error $\epsilon_{L_2}^l$	numerical convergence rate $\rho_{L_2}^l$
0	3117	$1.407\ 10^{-2}$	$9.7146\ 10^{-7}$	
1	12446	$6.7177\ 10^{-3}$	$2.6754\ 10^{-7}$	1.7443
2	49669	$3.5017\ 10^{-3}$	$7.0362\ 10^{-8}$	2.0501
3	198212	$1.7503\ 10^{-3}$	$1.857\ 10^{-8}$	1.9210
4	795195	$8.998\ 10^{-4}$	$4.5971\ 10^{-9}$	2.0983

Table 1: L_2-error and numerical convergence rate of the finite volume scheme for the numerical solution of (4.1) with anisotropy coefficients $(\alpha_r, \alpha_z) = (10, 1)$.

In Figures 4 and 5, we present isolevel plots of our two numerical solutions of (4.1) in comparison with the isolevel plots of the corresponding exact solution. In these plots, even for the coarsest grid, the numerical solution is virtually indistinguishable from the exact solution.

level l	number of triangles	max edge length h^l	L_2-error $\epsilon^l_{L_2}$	numerical convergence rate $\rho^l_{L_2}$
0	3117	1.407 10^{-2}	6.8619 10^{-7}	
1	12446	6.7177 10^{-3}	1.7805 10^{-7}	1.8248
2	49669	3.5017 10^{-3}	4.8672 10^{-8}	1.9907
3	198212	1.7503 10^{-3}	1.3105 10^{-8}	1.8921
4	795195	8.998 10^{-4}	3.1317 10^{-9}	2.1513

Table 2: L_2-error and numerical convergence rate of the finite volume scheme for the numerical solution of (4.1) with anisotropy coefficients $(\alpha_r, \alpha_z) = (1, 10)$.

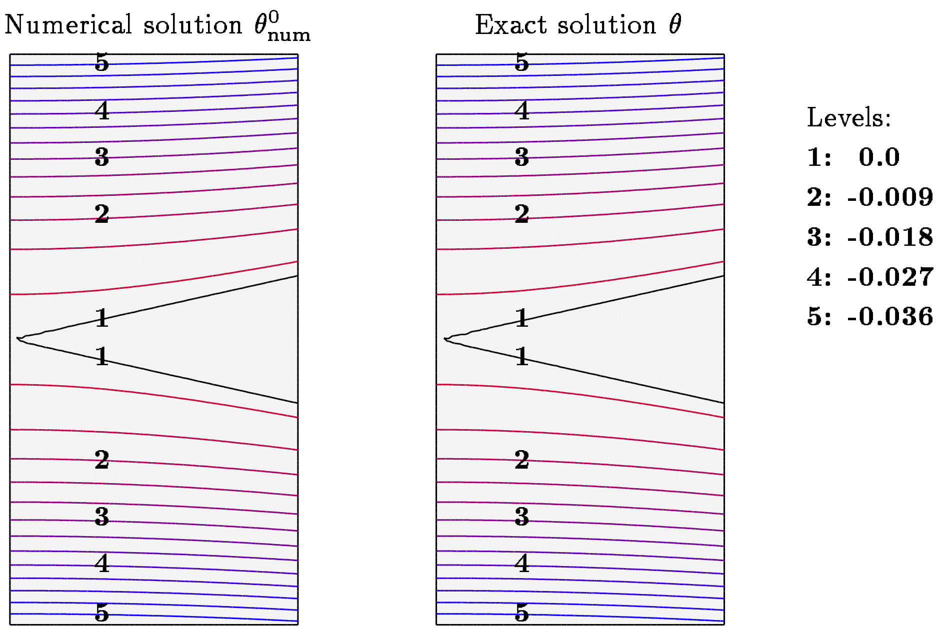

Figure 4: Isolevel plots on $\Omega = (0, 0.2) \times (-0.2, 0.2)$ of the numerical solution θ^0_{num} (grid level 0: 3117 triangles) (left) and of the exact solution θ (right) of the Dirichlet problem (4.1) with anisotropy coefficients $(\alpha_r, \alpha_z) = (10, 1)$. The difference between neighboring isolevels is 0.003.

4.2.2 Multi-material domain

For further verification of our method, we consider an axisymmetric Dirichlet problem with a closed-form solution, where the rectangular domain Ω decomposes into four materials Ω_m, $m \in \{1, 2, 3, 4\}$, each material having different anisotropy coefficients $(\alpha_{m,r}, \alpha_{m,z})$. More precisely, in cylindrical coordinates (r, z), we consider the following domains (see Fig. 6):

$$\Omega_1 = \{(r, z) : 0 < r < 0.1,\ 0 < z < 0.1\}, \quad \Omega_2 = \{(r, z) : 0.1 < r < 0.2,\ 0 < z < 0.1\},$$
$$\Omega_3 = \{(r, z) : 0 < r < 0.1,\ 0.1 < z < 0.2\}, \quad \Omega_4 = \{(r, z) : 0.1 < r < 0.2,\ 0.1 < z < 0.2\},$$

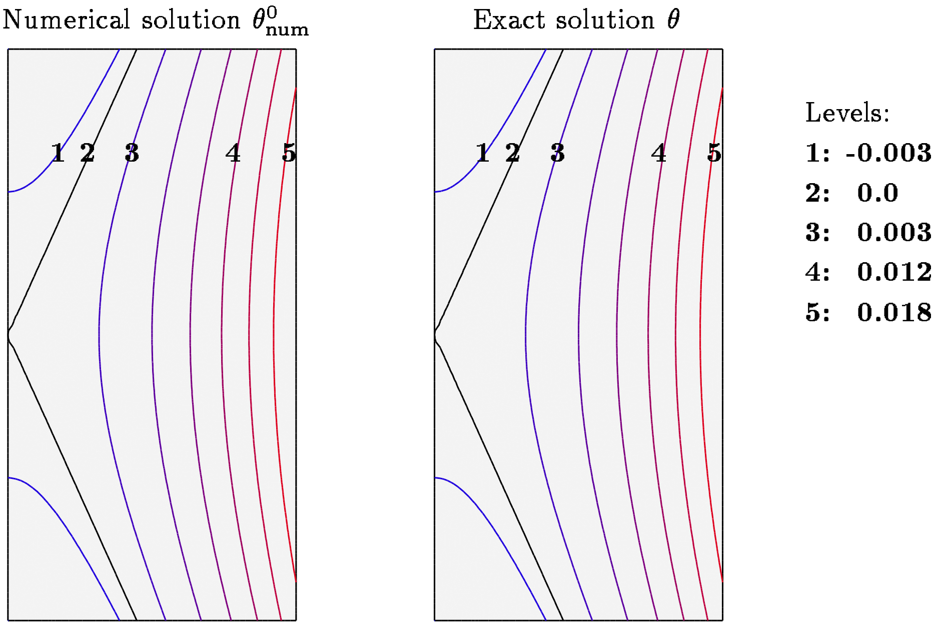

Figure 5: Isolevel plots on $\Omega = (0, 0.2) \times (-0.2, 0.2)$ of the numerical solution $\theta^0_{\rm num}$ (grid level 0: 3117 triangles) (left) and of the exact solution θ (right) of the Dirichlet problem (4.1) with anisotropy coefficients $(\alpha_r, \alpha_z) = (1, 10)$. The difference between neighboring isolevels is 0.003.

and, given positive coefficients $(\alpha_{m,r}, \alpha_{m,z})$ and real coefficients (a_m, b_m, c_m, f_m) for each $m \in \{1, 2, 3, 4\}$, we consider the Dirichlet problem

$$-\frac{1}{r}\frac{\partial}{\partial r}\left(r\,\alpha_{m,r}\,\frac{\partial\theta}{\partial r}\right) - \frac{\partial}{\partial z}\left(\alpha_{m,z}\,\frac{\partial\theta}{\partial z}\right) = f_m \quad \text{in } \Omega_m, \tag{4.7a}$$

$$\left(\begin{pmatrix}\alpha_{m,r} & 0\\ 0 & \alpha_{m,z}\end{pmatrix}\nabla\theta\restriction_{\Omega_m}\right)\bullet\mathbf{n}_m = \left(\begin{pmatrix}\alpha_{\tilde m,r} & 0\\ 0 & \alpha_{\tilde m,z}\end{pmatrix}\nabla\theta\restriction_{\Omega_{\tilde m}}\right)\bullet\mathbf{n}_m \quad \text{on } \partial\Omega_m\cap\partial\Omega_{\tilde m}, \tag{4.7b}$$

$$\theta(r,z) = \theta_{\mathrm{Dir},m}(r,z) := a_m\,r^2 + b_m\,z^2 + c_m \quad \text{on } \partial\Omega\cap\partial\Omega_m, \tag{4.7c}$$

where θ is required to be continuous throughout $\overline{\Omega}$. From the ansatz

$$\theta(r,z) := a_m\,r^2 + b_m\,z^2 + c_m \qquad \text{on } \overline{\Omega}_m, \quad m \in \{1,2,3,4\}, \tag{4.8}$$

it is readily verified that (4.8) provides the exact solution to (4.7) if the coefficients $\alpha_{m,r}$, $\alpha_{m,z}$, a_m, b_m, c_m, and f_m are chosen as follows:

$$\begin{array}{llll}
\alpha_{1,r} = 2, & \alpha_{2,r} = 1, & \alpha_{3,r} = 4, & \alpha_{4,r} = 2,\\
\alpha_{1,z} = 1, & \alpha_{2,z} = 2, & \alpha_{3,z} = 3, & \alpha_{4,z} = 6,\\
a_1 = 1, & a_2 = 2, & a_3 = 1, & a_4 = 2,\\
b_1 = 1, & b_2 = 1, & b_3 = 1/3, & b_4 = 1/3,\\
c_1 = 0, & c_2 = -1/100, & c_3 = 2/300, & c_4 = -1/300,\\
f_1 = -10, & f_2 = -12, & f_3 = -18, & f_4 = -20.
\end{array} \tag{4.9}$$

The values (4.9) are the ones we use in our numerical experiments.

As in the previous Sec. 4.2.1, we compute numerical solutions θ^l_{num} for grid levels l of increasing fineness to determine the numerical convergence rate. As before, we choose the area bounds $A^0 := 4\cdot 10^{-5}$, $A^l := (1/4)^l\, A^0$, $l \in \{0, \ldots, 4\}$, enforced by the grid generator. For each grid level l, we determine the actually occurring maximal edge length h^l according to (4.6) and compute the numerical convergence rate $\rho^l_{L_2}$ according to (4.5). Here, the discontinuity in the diffusion coefficients $(\alpha_{m,r}, \alpha_{m,z})$ across material interfaces results in the solution's gradient being discontinuous across material interfaces as well. In consequence, as compared to the results of the previous section, we lose one order of convergence, as can be seen from the values of the discrete L_2-error $\epsilon^l_{L_2}$ and the numerical convergence rate $\rho^l_{L_2}$ collected in Table 3: The error is approximately proportional to the maximal edge length in the space discretization. This corresponds to the order of convergence proved for some finite volume schemes in [EGH00, BMO96]. Moreover, since the solution is in $H^{1+s}(\Omega)$ for all $s < 1/2$ but not for $s = 1$, one may expect, after considering [Bey98, Satz 4.2.25], that one has convergence of order h^s for all $s < 1$, but not convergence of linear order.

In spite of the reduced convergence rate, Figure 6 shows that, as in the previous Sec. 4.2.1, even for the coarsest grid, the numerical solution is virtually indistinguishable from the exact solution.

level l	number of triangles	max edge length h^l	L_2-error $\epsilon^l_{L_2}$	numerical convergence rate $\rho^l_{L_2}$
0	1557	$1.271\ 10^{-2}$	$2.5600\ 10^{-5}$	
1	6148	$6.803\ 10^{-3}$	$1.2825\ 10^{-5}$	1.1059
2	24813	$3.4106\ 10^{-3}$	$6.3352\ 10^{-6}$	1.0214
3	99428	$1.793\ 10^{-3}$	$3.1972\ 10^{-6}$	1.0635
4	398130	$8.925\ 10^{-4}$	$1.6108\ 10^{-6}$	0.9827

Table 3: L_2-error and numerical convergence rate of the finite volume scheme for the numerical solution of (4.7) with the coefficients chosen according to (4.9).

Further tests with various sets of coefficients also confirm the convergence of our scheme. Thus, the next step is the application of the method to a complex geometry of a realistic application, where a closed-form solution is no longer available. We consider such an application in the following Sec. 4.3, namely the crystal growth apparatus presented in the Introduction (see Fig. 1).

4.3 Results for complex geometry

In this section, we apply the axisymmetric version of scheme (3.22) (cf. Sec. 3.6) to compute numerical solutions to the nonlinear stationary anisotropic heat equation (2.1) on the axisymmetric domain Ω depicted in Fig. 1. The radius is 12 cm and the height is 45.3 cm. As described in the Introduction, this domain represents a growth

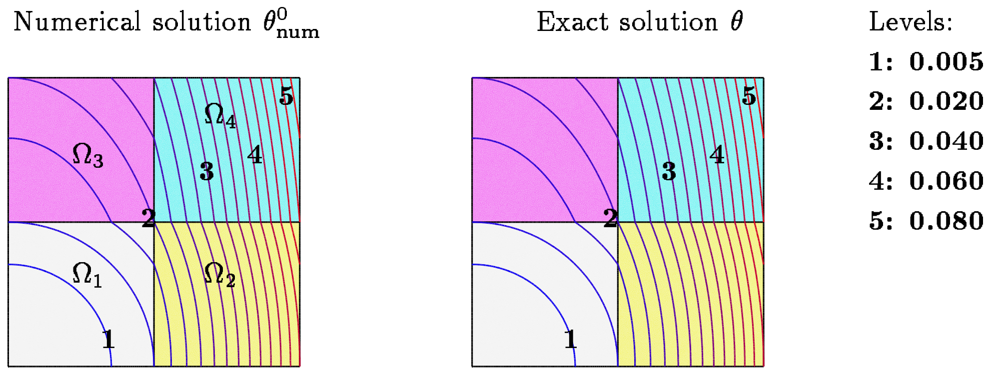

Figure 6: Isolevel plots on $\Omega = (0, 0.2) \times (0, 0.2)$ of the numerical solution θ^0_{num} (grid level 0: 1557 triangles) (left) and of the exact solution θ (right) of the Dirichlet problem (4.7) with the coefficients chosen according to (4.9). The difference between neighboring isolevels is 0.005.

apparatus used in silicon carbide single crystal growth by the PVT method. As shown in Fig. 1, Ω consists of six subdomains Ω_m, $m \in \{1, \dots, 6\}$, representing the materials insulation, graphite crucible, SiC crystal seed, gas enclosure, SiC powder source, and quartz. Aiming to use realistic functions for the isotropic parts $\kappa^m_{\text{iso}}(\theta)$ of the thermal conductivity tensors (cf. (2.2)), for gas enclosure, graphite crucible, insulation, and SiC crystal seed, we use the functions given by (A.1), (A.3b), (A.4b), and (A.7b) in [KPSW01]; for $\kappa^5_{\text{iso}}(\theta)$ (SiC powder source), we use [KP03, (A.1)], and for $\kappa^6_{\text{iso}}(\theta)$ (quartz), we use

$$\kappa^6_{\text{iso}}(\theta) = \left(1.82 - 1.21 \cdot 10^{-3}\,\frac{\theta}{\mathrm{K}} + 1.75 \cdot 10^{-6}\,\frac{\theta^2}{\mathrm{K}^2}\right) \frac{\mathrm{W}}{\mathrm{m\,K}}. \tag{4.10}$$

Hence, all functions $\kappa^m_{\text{iso}}(\theta)$ depend nonlinearly on θ. As mentioned in the Introduction, the thermal conductivity in the insulation is typically anisotropic in PVT growth apparatus. In the numerical experiments reported on below, we therefore vary the anisotropy coefficients (α^1_r, α^1_z) of the insulation while keeping $(\alpha^m_r, \alpha^m_z) = (1, 1)$ for all other materials $m \in \{2, \dots, 5\}$.

Heat sources $f_m \neq 0$ are supposed to be present *only* in the part of Ω_2 (graphite crucible) labeled by "uniform heat sources" in the left-hand picture in Fig. 7 satisfying 5.4 cm $\leq r \leq$ 6.6 cm and 9.3 cm $\leq z \leq$ 42.0 cm. In that region, f_2 is set to the constant value $f_2 = 1.23$ MW/m^3, which corresponds to a total heating power of 1.8 kW. This serves as an approximation to the situation typically found in a radio frequency induction-heated apparatus, where a moderate skin effect concentrates the heat sources within a few millimeters of the conductor's outer surface.

The interface conditions are given by (2.3). Here, our main goal is to illustrate the effectiveness of our finite volume scheme of Sec. 3 to compute the temperature field in a realistic complex geometry involving materials with anisotropic thermal conductivity. If the anisotropy in the thermal conductivity of the insulation is sufficiently large, we expect the isotherms to be almost parallel to the direction with the larger anisotropy coefficient. Since using the Dirichlet boundary condition (2.4a) can suppress such an alignment of the isotherms, we opt to use the Robin condition (2.4b) on all of $\partial\Omega$ instead. For $m \in \{1, 2, 6\}$, we set $\theta_{\text{ext},m} = 500$ K and $\xi_m = 80$ W/(m^{2}K) (recall from Fig. 1 that Ω_1, Ω_2, and Ω_6 represent the insulation, the graphite crucible, and quartz, respectively, and, thus, the outer materials of the apparatus).

The setting of this section constitutes a compromise between showing a realistic situation and staying within the scope of the simple model of Sec. 2. More realistic computations of heat transfer in PVT growth apparatus involve simulations at higher temperatures, computing the heat sources by solving Maxwell's equations, and including nonlocal radiative heat transfer between cavity surfaces as well as Stefan-Boltzmann emission conditions. For results of such numerical simulations, also applying the finite volume scheme developed in the current article to handle anisotropic thermal conductivity, we refer to our paper [GKP05].

We now present results of 7 numerical experiments, varying the anisotropy coefficients (α_r^1, α_z^1) in the insulation. In each case, we use a fine grid consisting of 61 222 triangles. We start with the isotropic case $(\alpha_r^1, \alpha_z^1) = (1, 1)$ depicted on the right-hand side of Fig. 7. Figure 8 shows the computed temperature fields for the moderately anisotropic cases $(\alpha_r^1, \alpha_z^1) = (10, 1)$ (left), $(\alpha_r^1, \alpha_z^1) = (1, 10)$ (middle), $(\alpha_r^1, \alpha_z^1) = (10, 1)$ in top and bottom insulation parts, $(\alpha_r^1, \alpha_z^1) = (1, 10)$ in insulation side wall (right). Figure 9 shows the computed temperature fields for the strongly anisotropic cases $(\alpha_r^1, \alpha_z^1) = (1000, 1)$ (left), $(\alpha_r^1, \alpha_z^1) = (1, 1000)$ (middle), $(\alpha_r^1, \alpha_z^1) = (1000, 1)$ in top and bottom insulation parts, $(\alpha_r^1, \alpha_z^1) = (1, 1000)$ in insulation side wall (right). The maximal temperatures established in the 7 experiments are collected in Table 4.

α_r^1	α_z^1	maximal temperature $[K]$
1	1	1273.18
1	10	1232.15
1-10, mixed	1-10, mixed	1238.38
10	1	918.35
1	1000	1063.58
1-1000, mixed	1-1000, mixed	1030.45
1000	1	706.36

Table 4: Maximal temperatures for the 7 numerical experiments discussed in Sec. 4.3, depending on the anisotropy coefficients (α_r^1, α_z^1) of the insulation (cf. Figures 7 - 9).

Comparing the temperature fields in Figures 7 - 9 as well as the maximal temperatures listed in Table 4, we find that any anisotropy reduces the effectiveness of the thermal insulation, where a stronger anisotropy results in less insulation: As we keep the total heating power fixed at 1.8 kW in each experiment, lower temperatures in the apparatus indicate a less effective thermal insulation. Here, the effect

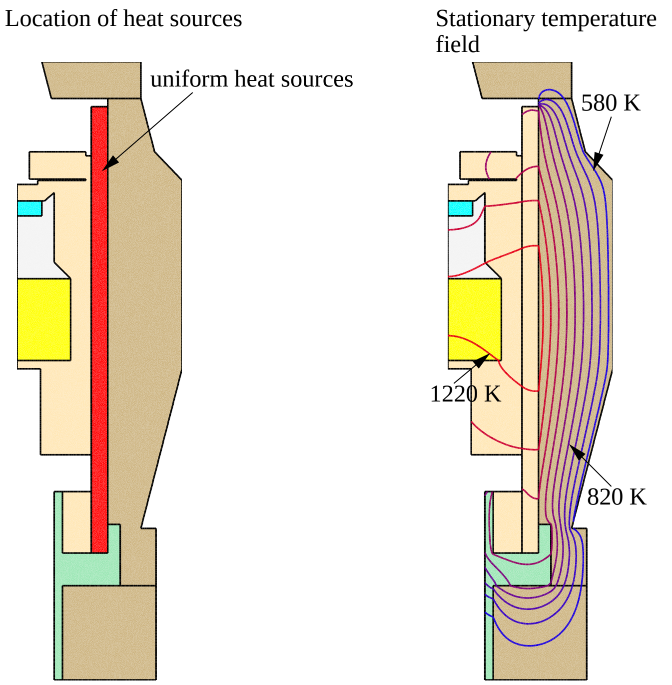

Figure 7: Left: Location of the heat sources. Right: Computed temperature field for the isotropic case $\alpha_r^1 = \alpha_z^1 = 1$, where the isotherms are spaced at 80 K.

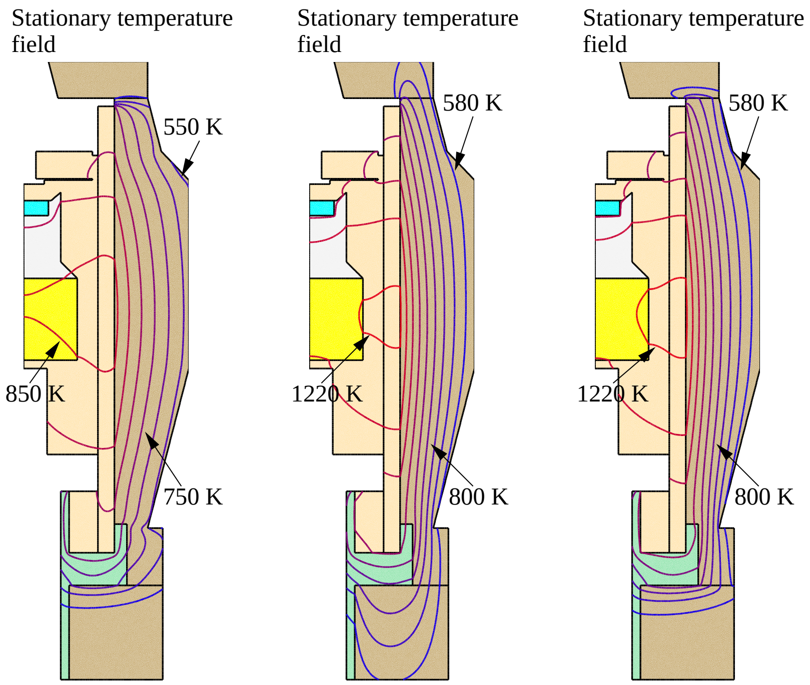

Figure 8: Computed temperature fields for the moderately anisotropic cases $(\alpha_r^1, \alpha_z^1) = (10, 1)$ (left, isotherms spaced at 50 K); $(\alpha_r^1, \alpha_z^1) = (1, 10)$ (middle, isotherms spaced at 80 K); $(\alpha_r^1, \alpha_z^1) = (10, 1)$ in top and bottom insulation parts, $(\alpha_r^1, \alpha_z^1) = (1, 10)$ in insulation side wall (right, isotherms spaced at 80 K).

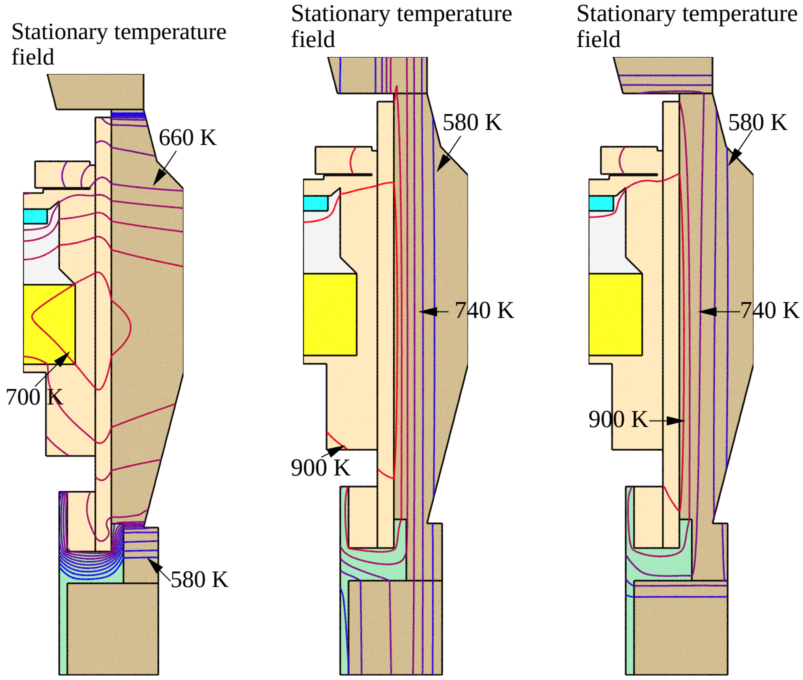

Figure 9: Computed temperature fields for the strongly anisotropic cases $(\alpha_r^1, \alpha_z^1) = (1000, 1)$ (left, isotherms spaced at 10 K); $(\alpha_r^1, \alpha_z^1) = (1, 1000)$ (middle, isotherms spaced at 80 K); $(\alpha_r^1, \alpha_z^1) = (1000, 1)$ in top and bottom insulation parts, $(\alpha_r^1, \alpha_z^1) = (1, 1000)$ in insulation side wall (right, isotherms spaced at 80 K).

that a stronger anisotropy results in a less effective insulation is expected, since raising the anisotropy coefficients of one direction to a value above 1 improves the insulation's thermal conductivity in that direction. Similarly, when reducing one of the anisotropy coefficients to a value below 1, a stronger anisotropy would result in improved insulation.

It can also be seen from Figures 7 - 9 and Table 4 that the insulation's effectiveness depends strongly on the orientation of the anisotropy: Raising α_r^1 to 10 and 1000 has a much more pronounced effect than raising α_z^1 to 10 and 1000. The reason is that a large thermal conductivity in the radial direction results in heat being effectively transported from the region of the heat sources to the vertical boundary of the apparatus. When constructing the apparatus it is thus important to use the insulation material such that its preferred direction of thermal conductivity is parallel to the side wall. Changing the anisotropy orientation in the top and bottom parts of the insulation (right-hand side in Figures 8 and 9) seems to have little effect on the overall temperature field. However, the temperature field *inside* the top and bottom parts of the insulation is affected considerably by changing the parts' anisotropy. In particular, one can clearly see the expected alignment of the isotherms with the preferred direction of thermal conductivity. Moreover, for the strongly anisotropic cases (Fig. 9), the isotherms' alignment is quite prominent in all three considered cases.

5 Conclusions

We have constructed a finite volume scheme suitable for the solution of nonlinear heat equations with anisotropic thermal conductivity on complicated polyhedral domains. The discretization of the space domains is facilitated by unstructured grids, namely triangulations satisfying the constrained Delaunay condition. The finite volume scheme is described for Cartesian coordinates as well as for cylindrical coordinates to allow the application to axisymmetric geometries. The scheme has been verified in comparison with exact closed-form solutions, showing second order convergence in a single-material domain and first order convergence in a multi-material domain with jumping thermal conductivity coefficients. Furthermore, the finite volume scheme has been applied to compute the heat transport in a complex crystal growth apparatus using various anisotropic thermal conductivities in its insulation, demonstrating the effectiveness of the method in realistic applications.

6 Acknowledgments

We thank Jürgen Fuhrmann and Klaus Gärtner (WIAS Berlin) for helpful discussions and advice.

References

[ABB98a] I. Aavatsmark, T. Barkve, Ø. Bøe, and T. Mannseth. *Discretization on unstructured grids for inhomogeneous, anisotropic media. Part I: Derivation of the methods.* SIAM J. Sci. Comput. **19** (1998), No. 5, 1700–1716.

[ABB98b] I. Aavatsmark, T. Barkve, Ø. Bøe, and T. Mannseth. *Discretization on unstructured grids for inhomogeneous, anisotropic media. Part II: Discussion and numerical results.* SIAM J. Sci. Comput. **19** (1998), No. 5, 1717–1736.

[BMO96] J. Baranger, J.F. Maitre, and F. Oudin. *Connection between finite volume and mixed finite element methods.* Math. Model. Numer. Anal. **30** (1996), No. 4, 335–465.

[Bey98] J. Bey, *Finite-Volumen- und Mehrgitterverfahren für elliptische Randwertprobleme.* B.G. Teubner, Stuttgart, Leibzig, Germany, 1998. In German.

[BV03] I. Braianov and L. Volkov, *Numerical solution of a reaction-diffusion elliptic interface problem with strong anisotropy*, Computing **71** (2003), 153–173.

[CLZ02] Z. CHEN, R. LI and A. ZHOU. *A note on the optimal L^2-estimate of the finite volume element method.* Adv. Comput. Math. **16** (2002), 291–303.

[CL91] P.G. CIARLET and J.L. LIONS (eds.). *Finite Element Methods (Part 1).* Handbook of Numerical Analysis, Vol. II, North-Holland/ Elsevier, Amsterdam, The Netherlands, 1991.

[DNR+90] F. DUPRET, P. NICODÉME, Y. RYCKMANS, P. WOUTERS, and M.J. CROCHET. *Global modelling of heat transfer in crystal growth furnaces.* Intern. J. Heat Mass Transfer **33** (1990), No. 9, 1849–1871.

[EGH00] R. EYMARD, T. GALLOUËT, and R. HERBIN. *Finite volume methods*, pp. 713–1020 in P.G. CIARLET and J.L. LIONS (eds.). *Solution of Equations in $\mathbb{R}^n$ (Part 3); Techniques of Scientific Computing (Part 3).* Handbook of Numerical Analysis, Vol. VII, North-Holland / Elsevier, Amsterdam, The Netherlands, 2000.

[Fai91] I. FAILLE, *A control volume method to solve an elliptic equation on a two-dimensional irregular mesh*, Computer Methods in Applied Meachanics and Engineering **100** (1992), pp. 275–290.

[FKL01] J. FUHRMANN, TH. KOPRUCKI, and H. LANGMACH. *pdelib: An open modular tool box for the numerical solution of partial differential equations. Design patterns*, in W. HACKBUSCH and G. WITTUM (eds.). *Proceedings of the 14th GAMM Seminar on Concepts of Numerical Software, Kiel, January 23–25, 1998.* University of Kiel, Germany, 2001.

[FL01] J. FUHRMANN and H. LANGMACH. *Stability and existence of solutions of time-implicit finite volume schemes for viscous nonlinear conservation laws.* Applied Numerical Mathematics **37** (2001), No. 1–2, 201–230.

[For01] V.F. FORMALEV. *Heat and mass transfer in anisotropic bodies.* High Temperature **39** (2001), No. 5, 753–774.

[GKP05] J. GEISER, O. KLEIN, and P. PHILIP. *Anisotropic thermal conductivity in apparatus insulation: Numerical study of effects on the temperature field during sublimation growth of silicon carbide single crystals.* In preparation.

[KP02] O. KLEIN and P. PHILIP. *Correct voltage distribution for axisymmetric sinusoidal modeling of induction heating with prescribed current, voltage, or power.* IEEE Trans. Mag. **38** (2002), No. 3, 1519–1523.

[KP03] O. KLEIN and P. PHILIP. *Transient temperature phenomena during sublimation growth of silicon carbide single crystals.* J. Crystal Growth **249** (2003), No. 3–4, 514–522.

[KP05] O. KLEIN and P. PHILIP. *Transient conductive-radiative heat transfer: Discrete existence and uniqueness for a finite volume scheme.* Math. Mod. Meth. Appl. Sci. **15** (2005), No. 2, 227–258.

[KPS04] O. KLEIN, P. PHILIP, and J. SPREKELS. *Modeling and simulation of sublimation growth of SiC bulk single crystals.* Interfaces and Free Boundaries **6** (2004), 295–314.

[KPSW01] O. KLEIN, P. PHILIP, J. SPREKELS and K. WILMAŃSKI. *Radiation- and convection-driven transient heat transfer during sublimation growth of silicon carbide single crystals.* J. Crystal Growth **222** (2001), No. 4, 832–851.

[Krö97] D. KRÖNER. *Numerical Schemes for Conservation Laws.* Advances in Numerical Mathematics, Wiley Teubner, Chichester, UK, Stuttgart, Germany, 1997.

[LeV02] R.J. LEVEQUE. *Finite Volume Methods for Hyperbolic Problems.* Cambridge Texts in Applied Mathematics, Cambridge University Press, 2002.

[Phi03] P. PHILIP. *Transient Numerical Simulation of Sublimation Growth of SiC Bulk Single Crystals. Modeling, Finite Volume Method, Results.* Ph.D. thesis, Department of Mathematics, Humboldt University of Berlin, Germany, 2003, Report No. 22, Weierstraß-Institut für Angewandte Analysis und Stochastik, Berlin.

[SG04] O. SCHENK and K. GÄRTNER. *Solving unsymmetric sparse systems of linear equations with PARDISO.* Journal of Future Generation Computer Systems **20** (2004), No. 3, 475–487.

[SGF00] O. SCHENK, K. GÄRTNER, and W. FICHTNER. *Scalable parallel sparse factorization with left-strategy on shared memory multiprocessor.* BIT **40** (2000), No. 1, 158–176.

[She96] J.R. SHEWCHUK. *Triangle: Engineering a 2D quality mesh generator and delaunay triangulator*, in *First Workshop on Applied Computational Geometry (Philadelphia, Pennsylvania).* ACM, May 1996, pp. 124–133.

[SSP04] K. SEMMELROTH, N. SCHULZE, and G. PENSL. *Growth of SiC polytypes by the physical vapour transport technique.* J. Phys.-Condes. Matter **16** (2004), S1597–S1610.